

Bullet pressure-cell design for neutron scattering experiments with horizontal magnetic fields and dilution temperatures

Ellen Fogh*, Gaétan Girit, Richard Gaal, Luc Testa, Jana Pásztorová, and Henrik M. Rønnow
*Laboratory for Quantum Magnetism, Institute of Physics,
 École Polytechnique Fédérale de Lausanne (EPFL), CH-1015 Lausanne, Switzerland*

Oleksandr Prokhnenko and Maciej Bartkowiak
Helmholtz-Zentrum Berlin für Materialien und Energie, D-14109 Berlin, Germany

Ekaterina Pomjakushina
*Laboratory for Multiscale Materials Experiments, PSI Center for Neutron and Muon Sciences,
 Forschungsstrasse 111, 5232 Villigen PSI, Switzerland*

Yoshiya Uwatoko
Institute for Solid State Physics (ISSP), University of Tokyo, Kashiwa, Chiba 277-8581, Japan

Hiroyuki Nojiri
Institute for Materials Research, Tohoku University, Sendai 980-8577, Japan

Koji Munakata and Kazuhisa Kakurai
*Neutron Science and Technology Center, Comprehensive Research Organization
 for Science and Society (CROSS), Tokai, Ibaraki 319-1106, Japan
 (*ellen.fogh@epfl.ch)
 (Dated: April 17, 2025)*

The simultaneous application of high magnetic fields and high pressures for controlling magnetic ground states is important for testing our understanding of many-body quantum theory. However, the implementation for neutron scattering experiments presents a technical challenge. To overcome this challenge we present an optimized pressure-cell design with a novel bullet shape, which is compatible with horizontal-field magnets, in particular the high-field magnet operating at the Helmholtz-Zentrum Berlin. The cell enabled neutron diffraction and spectroscopy measurements with the combination of three extreme conditions: high pressures, high magnetic fields, and dilution temperatures, simultaneously reaching 0.7 GPa, 25.9 T, and 200 mK. Our results demonstrate the utility of informed material choices and the efficiency of finite-element analysis for future pressure-cell designs to be used in combination with magnetic fields and dilution temperatures for neutron scattering purposes.

I. INTRODUCTION

To map out phase diagrams and to characterize critical behavior close to quantum phase transitions it is essential to be able to control applied magnetic fields, hydrostatic pressures and temperatures simultaneously during an experiment. The Zeeman term in the spin Hamiltonian is exact and the magnetic field strength may be tuned accurately *in situ*. Hydrostatic pressure is a means of manipulating interatomic bond lengths and angles and thereby alter magnetic interactions while preserving the chemical composition. Many quantum magnets require low temperatures to reach the interesting part of their phase diagrams [1, 2]. Finally, neutron scattering is a unique technique for studying spin correlations directly [3] and because neutrons penetrate matter easily compared to other scattering probes, such as X-rays or electrons, it is possible to have large equipment for controlling the sample environment. Therefore, neutron scattering experiments for studying quantum magnetic systems under applied magnetic field and pressures and at low temperatures constitute an extremely powerful tool.

An overview of capabilities at different neutron scattering

facilities is presented in Table I and illustrated in Fig. 1. To our best knowledge the record for combining all three extremes of high pressure, high magnetic fields and low temperatures is 2.8 GPa, 7 T and 0.1 K [15]. Disregarding pressure for a moment, a combination of a dilution refrigerator and a standard vertical superconducting cryomagnet provides routinely 15 T and 50 mK, which gives access to the (H, T) phase diagram of many systems. Until the end of 2019 a High Field Magnet (HFM) facility for neutron scattering was operated at the Extreme Environment Diffractometer (EXED) at the Helmholtz-Zentrum Berlin (HZB) [17–20]. The hybrid magnet consisted of a resistive and a superconducting coil, which together with a bespoke dilution refrigerator, built in collaboration with the University of Birmingham, provided field strengths up to 25.9 T and temperatures down to 200 mK at the sample position. However, combining low temperatures with applied pressures is more challenging because of the power required to cool the pressure cell, which is typically a large piece of metal. Apart from aforementioned record, this has been achieved and documented in literature down to 1.4 K for pressures up to 43 GPa [21], down to 1.5 K for pressures up to 1.0 GPa [22, 23], down to 4.2 K for pressures

TABLE I. Overview of capabilities for combining high pressures, high magnetic fields, and low temperatures ($< 10\text{ K}$) at different neutron scattering facilities (non-exhaustive list). The available sample space is also listed for each pressure cell. Note that the listed pressures are the values at room temperature. Figure 1 represents these data in a graphical format.

Facility	Cell type	Pressure (GPa)	Magnetic field (T)	Temperature (K)	Sample space (mm ³)
ISIS [4, 5]	Clamp	1.75	9	1.8	390
ILL [6]	P.-E.	6.0	—	1.5	48
	Gas	0.7	6	1.5	1980
	McWhan (under repair)	3	—	0.5	35
PSI [7, 8]	Clamp	3.0	11	0.020	785
	P.-E.	5.5	—	6	21
JRR-3 [9–11]	Clamp	2.0	—	0.8	7
	Hybrid anvil	10	10	3	0.2
JRR-3 / HFIR [12]	Cubic anvil	7.0	—	3	1
J-PARC [13]	Clamp	1.8	—	0.1	25
IBR-2 [14]	Sapphire anvil	12	—	4	0.1
	Diamond anvil	50	—	4	0.01
LLB [15, 16] (until end of 2019)	Sapphire anvil	12	7.5	0.1	0.1
	Diamond anvil	50	—	1.4	0.01
HZB (until end of 2019)	Bullet	1.0	25.9	0.200	450

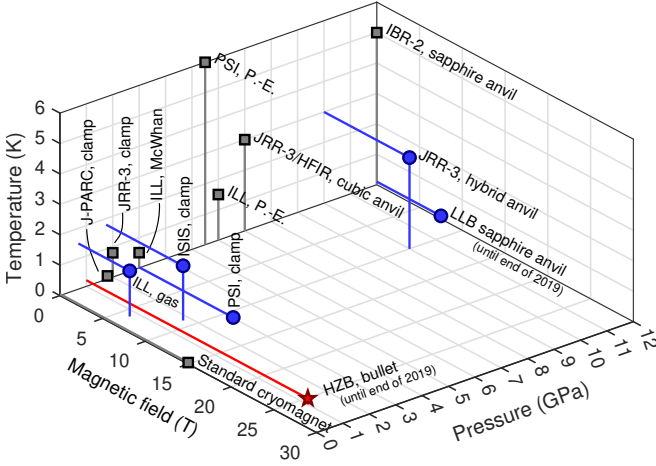


FIG. 1. Representation of capabilities listed in Table I. Black squares denote possibilities for combining low temperature with applied pressures or magnetic fields. Blue circles denote pressure cells with the possibility of combination with a magnetic field, i.e. the application of all three extremes. The red star is the bullet cell developed for the HFM/EXED instrument. Horizontal and vertical lines illustrate where the data points connect with the basal planes. Note that the 50 GPa “Kurchatov-LLB” diamond-anvil cell is omitted from this plot.

up to 6.0 GPa [24, 25], and down to 1.8 K for pressures up to 20.0 GPa [26], depending on the type of pressure cell and the type of measurement. Another challenge with regards to neutron scattering experiments in combination with high pressure is the rapidly decreasing sample space when demanding higher pressures. Therefore, these experiments are often feasible only for diffraction and when considering magnetic studies only for samples containing high-magnetic-moment ions typically found in rare earth compounds. Consequently, inelastic neutron studies of $S = 1/2$ systems under pressure are very few.

In this paper, we present a piston-cylinder pressure cell compatible with the dilution insert of the unique HFM/EXED instrument at the HZB. With an ultra-compact-cell design and optimized material choices, we succeeded in performing an inelastic neutron scattering experiment at 25.9 T, 0.7 GPa, and 200 mK, and in this way probing spin excitations under these extreme conditions. The novel bullet design, meaning with a dome shape on the outgoing neutron beam side, allows the scattered signal to escape in a wide range of angles and ensures uniform attenuation. The concept opens an alternative path to explore for future pressure-cell engineering for neutron scattering purposes, in particular in combination with horizontal magnetic fields.

II. OVERVIEW OF APPARATUS

The horizontal geometry and limited sample space of the 25.9 T magnet called for a highly specialized pressure-cell design. We used finite-element analysis as implemented in the software package ANSYS to simulate the pressure inside the cell and the strain on the components in order to optimize dimensions and material choices. The aim was to minimize the neutron background and attenuation, as well as to maximize the sample volume while obtaining 1.0 GPa at the sample position. Existing piston-cylinder cells typically consist of a vertical double-walled cylinder with pistons pushing from both top and bottom. In such cells, the neutrons travel through the cylinder walls in the transverse direction and not through the pistons. In the case of the spacially limited horizontal HFM, the neutrons were instead required to travel along the length of the cylinder. To minimize the neutron beam path through the pistons as well as to obtain uniform attenuation, we proposed a design consisting of a single piston assembly in the incoming beam path and a dome-shaped single wall at the other end. Due to this shape, it was named the “bullet” cell. A 3-dimensional (3D) representation and technical drawing of the

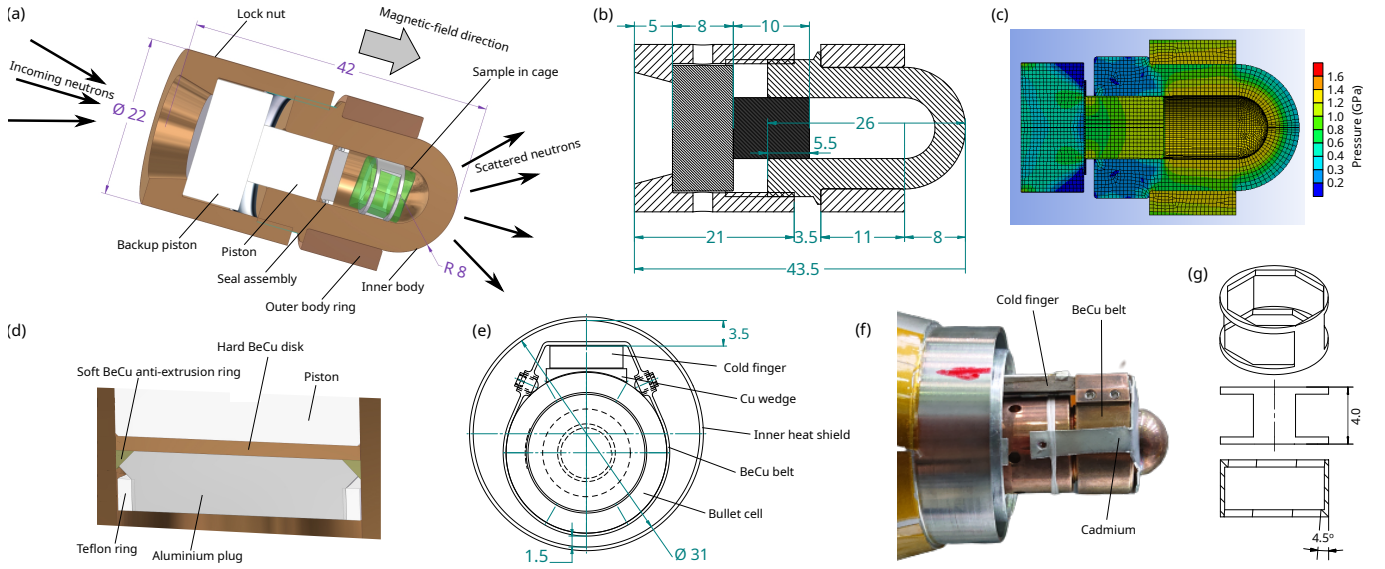


FIG. 2. **Pressure cell design.** Dimensions in all panels are given in millimeters. (a) 3D representation and (b) schematic drawing of the bullet cell (side view). (c) Color contours showing the pressure distribution at 1.2 GPa in the sample space as simulated using finite-element analysis. (d) Illustration of the seal assembly. (e) Schematic drawing of the cell mounted on the cold finger of the dilution refrigerator (front view). (f) Photograph of the cell mounted on the cold finger before closing the heat shields (side view). (g) Schematic drawings of the sample cage.

bullet cell are shown in Fig. 2(a)-(b) and a color contour representation of the pressure distribution is shown in Fig. 2(c).

The outer diameter of the cell is 22 mm with a sample space diameter of 8 mm. The sample space height is around 9 mm and the total length of the cell around 45 mm when closed. The exact dimensions when loaded depend on the piston displacement. The body of the cell is a double wall of hardened BeCu-25 with the outer support ring shrink fitted in place. The hardening of both body parts was carried out at 315°C in a nitrogen atmosphere to prevent oxidation. The dome-shaped part of the cell consists of a single wall, which allows more neutrons to escape when scattered from the sample compared to a double wall. This shape also provides an optimal force distribution, such that a single wall can support the required pressure. On the incoming-beam side, the locknut has a conical opening to allow rotation of the cell with respect to the incoming neutron beam. Ceramic ZrO₂ (Coorstek Technox 3000) is the material choice for the piston in order to minimize the absorption of incoming neutrons when they travel through the piston to reach the sample. The ceramic is more transparent to neutrons than, for example, tungsten carbide, but it is brittle compared to metallic BeCu. Therefore the piston is the limiting part in this design with regards to the maximum achievable pressure.

The seal assembly [Fig. 2(d)] consists of four parts: a teflon ring, an aluminum plug, a soft BeCu anti-extrusion ring and a hardened BeCu disk. The assembly seals directly against the wall of the bore so no sample can be required. It is necessary to polish the bore inside prior to loading in order to remove any scratches that may cause leaks. This was performed using a lathe and SiC grinding paper down to Grit 4000 (US #1200) and then diamond paste down to a grain size of 2 μm. This procedure was repeated for each loading, which means

that the bore gets slightly wider for each load and will eventually be too wide to be used with the same seal assembly and pistons. The anti-extrusion ring was covered with indium to create the initial seal. The slightly dome shaped BeCu disk inserted at the end serves to prevent the ceramic pistons from cracking by mediating the force more evenly over the surface.

All parts of the pressure cell, seal assembly and pistons were cleaned carefully using acetone and an ultrasound bath prior to loading. Afterwards, the sample was placed in the bore. The seal assembly was then prepared by squeezing the anti-extrusion ring with 120 kg on a hydraulic press using a steel ball with diameter 15 mm to achieve a slightly tighter fit inside the bore of the cell. The teflon ring was mounted on the aluminum plug. A deuterated 4:1 methanol-ethanol mixture was used as pressure medium and injected with a syringe to prevent air bubbles from becoming trapped under the sample. Deuterated methanol-ethanol was used to avoid the large incoherent neutron scattering associated with hydrogen [27], which generates an undesired addition to the background. In order to allow sufficient piston displacement for the required pressure while engaging enough thread to sustain the load on the locknut, a pressure-medium level of approximately 4 mm as measured from the top of the bore was optimal. The seal was then placed by first inserting the aluminum plug with the teflon ring and using a brass plate to push it in evenly. The anti-extrusion ring was placed on top and also pushed in with the brass plate. The BeCu disk was placed in the bore with the top of the dome on the piston side. The assembly was engaged using a tungsten (W720) dummy piston and loaded to 200 kg for initial sealing. Finally, pressure was applied using the ceramic pistons while making sure that all parts were well centered, ensuring an even load and that the locknut would fit the threads once the desired piston displacement had been

reached. Note that to minimize material, the locknut did not reach the thread of the cell body prior to loading. A holder fitted to the dome shape of the bullet cell body allowed us to carry out the loading on a standard hydraulic press. The load was increased slowly and continuously. Once the maximum load of 7200kg was reached the cell was monitored for approximately 1 h to ensure that all components stayed in place and no leaks appeared. The locknut was tightened 3 times to 7000kg, with the load topped up to 7200kg between each tightening. The duration of the press release was similar to the loading process while keeping track of the piston displacement in both directions. The loaded cell had a total mass of approximately 100g.

The cell was mounted on the cold finger of the dilution refrigerator for the HFM by using a BeCu belt of thickness 0.3mm, as shown in Figs. 2(e)-(f). To adapt from the flat surface of the cold finger to the rounded shape of the pressure cell, as well as to ensure thermal contact, a Cu wedge was inserted between the two surfaces. The wedge was gold plated on the curved side. The belt was tightened by engaging screws on either side. Cadmium masks were added on both the incoming and scattered beam sides to reduce the amount of illuminated cell material and to prevent neutrons scattered off the cell from reaching the detector.

Figure 3(a) shows the simulated diameter increase of the pressure cell as a function of the applied pressure. The curve deviates from linear behavior above around 1.1 GPa. The corresponding measured piston displacement as a function of applied load is shown for 7 individual loadings in Fig. 3(b). The loading curves are remarkably similar, regardless of the cell number and pressure medium. The linear behavior ends around 7000kg, which corresponds to 1.4 GPa at the sample position assuming no friction. Noting that the linear behavior of the piston displacement starts only around 1500kg, and allowing for some of the applied force being lost to friction, the simulation and experiment can be said to agree with each other. The fact that the loading curve is initially non-linear is explained by air trapped in the system, which has a much higher compressibility compared to the any of the pressure media used in our tests. Beyond a load of 7000kg, the BeCu deforms plastically. Especially the dome part of the cell with its single wall expands irregularly and does not revert to original size and shape upon depressurization. Note that upon cooling there is a substantial pressure loss of 30-50% (pressure determination at 200mK is treated in Section IV). Furthermore, once loaded the pressure was found to be leaking slowly (half life around 10 days with pressure fully lost after a month). This was observed by monitoring the decrease of the cell diameter over time. Consequently one needs to load the cell immediately before the experiment and cool it down without delay. Once the pressure medium is frozen, the pressure is conserved.

III. EXPERIMENT

The material of choice for testing the bullet pressure-cell design is the quantum magnet $\text{SrCu}_2(\text{BO}_3)_2$, which represents

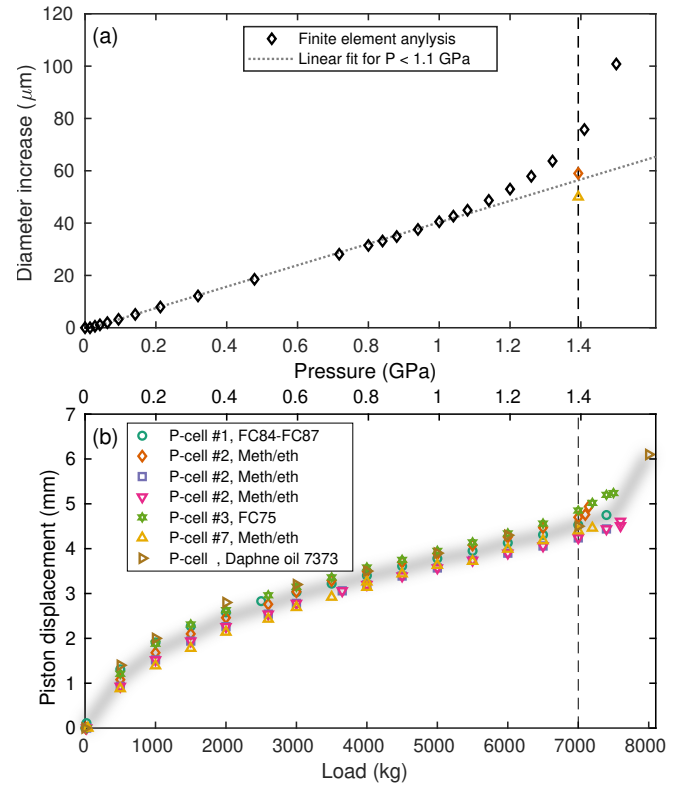


FIG. 3. **Pressure cell loading.** (a) Increase of the cell diameter as a function of applied pressure as simulated in ANSYS with a linear fit for $P < 1.1$ GPa. The red diamond and yellow triangle are experimentally measured increases of the diameter at an applied load of 7000 kg. (b) Piston displacement shown as a function of the applied load for 7 individual loadings using different copies of the cell as well as different pressure media. The dashed line indicates a load of 7000 kg where in the experiment the loading curve deviates from linear behavior. The gray shading is a guide to the eye.

a physical realization [28] of what is known as the Shastry-Sutherland model (SSM) [29]. The magnetic lattice consists of pairs of Cu^{2+} ($S = 1/2$) ions (dimers) arranged orthogonally to all neighboring pairs. The superexchange interactions are J within the dimer, and J' between dimers. At ambient conditions, $\text{SrCu}_2(\text{BO}_3)_2$ is well described by the SSM with $J'/J \approx 0.63$ [28, 30–34], and the ground state of the system is a product of singlets on the dimers [35–40]. Upon applying a magnetic field, a series of magnetization plateaus is observed [41–45] with the first of these occurring at 27 T. Here, the magnetization is 1/8 of its saturation value and a spin superstructure is predicted [46]. Torque measurements and numerical calculations indicate that applying pressure to $\text{SrCu}_2(\text{BO}_3)_2$ suppresses the transition field, bringing it below 25.9 T [44, 47, 48] and thus enabling a neutron scattering study of the 1/8 magnetization plateau in $\text{SrCu}_2(\text{BO}_3)_2$ by using a combination of the bullet cell and the HFM/EXED facility.

The HFM allowed for direct probing of the magnetic structure and dynamics up to 25.9 T static magnetic fields, the bullet cell provided a hydrostatic pressure of 0.7 GPa, and the

dilution insert took the system to a temperature of 200 mK. The magnet had 30° conical opening angles, which in combination with magnet rotation of $\omega \in [-11.8^\circ, +2^\circ]$ from the incident neutron beam and the time-of-flight (ToF) technique implemented on EXED, gave access to a substantial region in momentum transfer, $\mathbf{Q} = (q_h, q_k, q_l)$, and energy transfer, E . A schematic representation of the setup is shown in Fig. 4(a). For detailed descriptions and illustrations of this truly unique instrument and magnet we refer to Refs. 17–20. Three different chopper settings produced a wavelength band of $0.7 - 7.2 \text{ \AA}$ for diffraction and incoming energies $E_i = 4$ and 8 meV for inelastic measurements. A general characterization study of the bullet cell was performed by varying the magnet rotation angle. For collecting magnetic diffraction data we chose magnet rotation angle $\omega = 0$ and for inelastic measurements we positioned the magnet at $\omega = -6^\circ$. The latter angle was chosen as a compromise between access to a larger portion of reciprocal space and optimal neutron transmission through the pressure cell. Only forward scattering detectors were used in this experiment.

A single crystal of $\text{SrCu}_2(\text{BO}_3)_2$ grown by the floating-zone method [49, 50], was cut with octagonal cross section perpendicular to the \mathbf{c} -direction. This shape was chosen as a compromise between maximizing the sample volume in the cylindrical sample space and still being practical to cut. The resulting sample had a mass of 0.8 g and was mounted in an aluminum cage as shown in Fig. 2(a) and Fig. 2(g). The orientation of the $\text{SrCu}_2(\text{BO}_3)_2$ crystal was chosen to optimize the coverage in (\mathbf{Q}, E) . Multiple scenarios for sample and magnet orientations were simulated using the software packages EXEQ and InEXEQ, developed specifically for experiment planning at the HFM/EXED facility [51]. Theoretical calculations predict a spin texture with ordering vector in the $(q_h, q_k, 0)$ -plane for the $1/8$ magnetization plateau [46]. To observe this, the \mathbf{c} -direction of the crystal had to be tilted in the horizontal plane with respect to the magnetic field direction and with an optimal tilt angle of 4.5° . The sample cage was pre-cut to obtain this tilt angle [Fig. 2(g)]. The resulting sample orientation was determined by tracking nuclear Bragg peak positions on the detector upon magnet rotation.

IV. RESULTS

We start by examining the characterization results with a representative zero-field detector image shown in Fig. 4(b). The corresponding ToF intensity profiles for the observed nuclear Bragg peaks and reciprocal coverage are shown in Fig. 4(c)-(d). We point out that the irregular shape of the peaks in Fig. 4(c) are mainly due to intensity being spread over multiple detector tubes and to a lesser extent a result of sample mosaicity. Since the detector is constructed of arrays of vertical detector tubes with gaps in between some neutrons are not detected, but escape in between the tubes. This also explains why the shape of $(-2, -2, 0)$ appears more regular compared to $(-1, -1, 0)$ since it is spread over a smaller number of tubes.

All nuclear signals were observed for flight times below

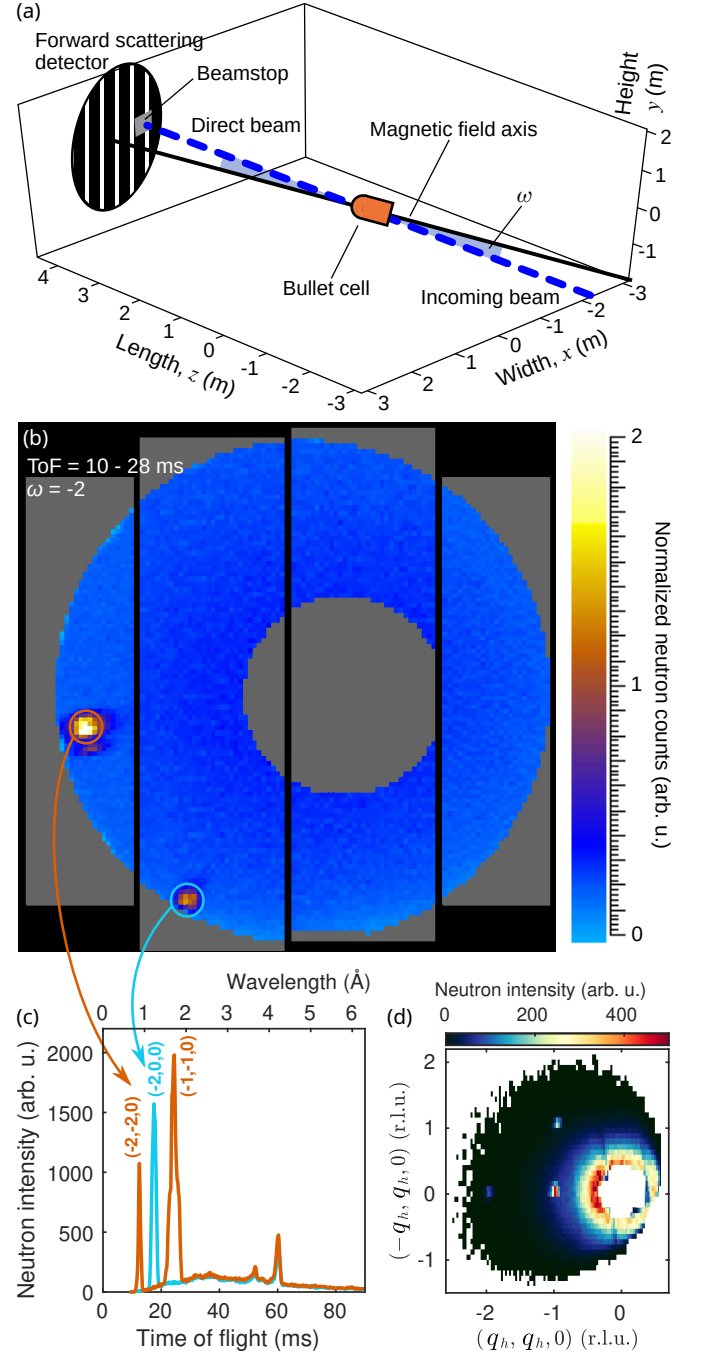


FIG. 4. Experimental setup and nuclear Bragg scattering. (a) Schematic representation of the instrument geometry, showing the magnetic-field axis (black line), the incoming-neutron-beam direction (dashed blue line), and the positions of the bullet cell and the detector. This image is based on simulations using the software package InEXEQ [51] (b) Detector image for magnet rotation $\omega = -2^\circ$ integrated over a ToF window of 10 – 28 ms. Two high-intensity spots are clearly visible in the lower left corner of the detector. The upper spot corresponds to the nuclear Bragg peaks $(-2, -2, 0)$ and $(-1, -1, 0)$ and the lower to $(-2, 0, 0)$. (c) Integrated neutron intensity at the detector positions of the two high-intensity spots shown as a function of neutron ToF. (d) Reciprocal space coverage corresponding to the detector image in panel (b).

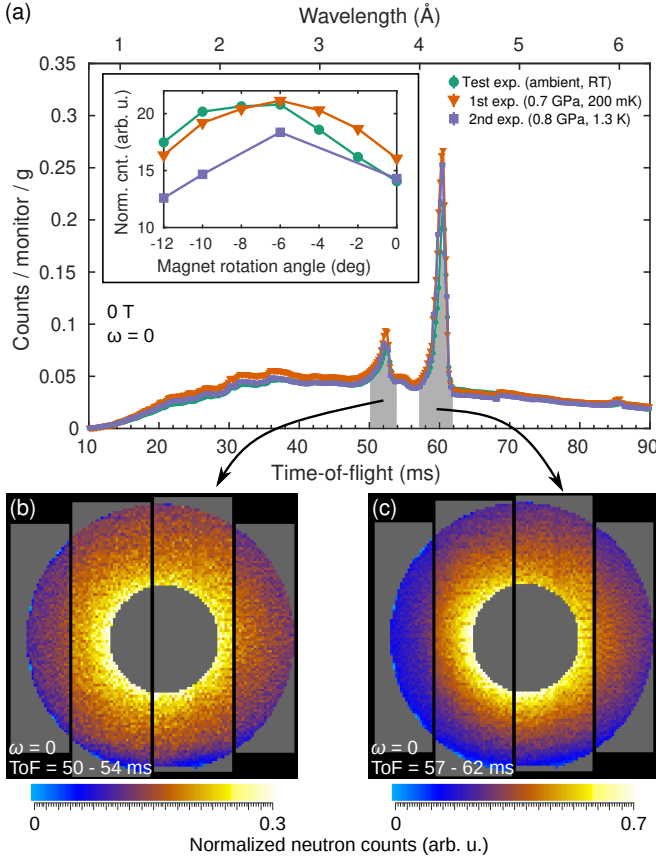


FIG. 5. **Background from the bullet cell.** (a) Neutron intensity shown as a function of ToF for three different pressure cells mounted on EXED and with no magnet rotation ($\omega = 0$). The neutron counts were summed over the entire detector excluding regions with nuclear Bragg peaks and normalized with respect to the sample mass. In the test experiment, the pressure cell was not loaded (but contained a sample) and the experiment was performed at room temperature (RT). The inset shows total neutron counts as integrated over all flight times and as a function of magnet rotation angle. The transmission has a maximum around $\omega = -6^\circ$. (b)-(c) Detector images for the two spurious around neutron flight times of 52 and 60 ms corresponding to the shaded areas in panel (a). The elevated level of neutron counts is distributed evenly throughout the detector in both cases.

40 ms. At larger flight times, around 52 and 60 ms, two additional peaks were observed. These are of spurious origin, as we demonstrate further below. To estimate the overall signal-to-noise performance of the bullet cell we did the following for each magnet rotation angle: (i) the Bragg peak intensities were determined by numerical integration over the relevant detector pixels and ToF intervals like in Fig. 4(b)-(c), (ii) the background signals were estimated by integrating parts of the detector for similarly located regions but away from any Bragg-peak intensity (not shown), and (iii) the signal-to-noise ratio was evaluated. The maximum signal-to-noise ratio obtained was around 8 times lower with the bullet cell in the beam compared to the ambient-pressure experiment performed without a pressure cell [52].

The total detector counts measured as a function of the neu-

tron ToF are shown in Fig. 5(a) for three different pressure cells and samples. Regions of the detector containing nuclear Bragg peak intensity were excluded and hence the curves in Fig. 5(a) represent the background, which is due largely to the pressure cell but also due to the cryostat and magnet. There are two prominent features at 52 and 60 ms on top of a very broad structure with maximum around 35 ms. These features are also clearly present in Fig. 4(b). The intensity around the peaks has no structure in Q [Fig. 5(b)-(c)] and are believed to originate from multiple scattering involving the BeCu pressure cell and one of the upstream aluminum windows. The spurious signal is likely enhanced by neutron transmission peaks around these wavelengths (3.6 and 4.1 Å) [53]. For potential future experiments at other neutron facilities as well as for future cell designs we will consider the approach in Ref. [54] using the Union framework [55] in the McStas Monte Carlo simulation package for neutron beamlines [56, 57] to identify possible spurious as well as ways to avoid them in experiments. Returning to the current cell design, the transmission is optimal around magnet rotation angle $\omega = -6^\circ$, which is why this particular angle was chosen for the inelastic neutron data collection. The small discrepancies between the curves in Fig. 5(a) (main panel and inset) are explained by slight differences in the cell orientation with respect to the incoming beam, which occur when mounting the cell on the cold finger. Note also that the data set at 1.3 K in Fig. 5(a) was collected using a different cryostat which explains the overall lower background counts.

The pressure was determined by the energy shift of the first triplet excitation in $\text{SrCu}_2(\text{BO}_3)_2$ at base temperature [Fig. 6]. The ambient-pressure reference was measured in a separate experiment without a pressure cell and a full treatment of these data is published elsewhere [52]. The integration ranges in Fig. 6 were $q_h = [-0.95, 0.55]$, $q_k = [-1.05, 0.45]$, $q_l = [-0.9, 1.3]$ for the curve at finite pressure and $q_h = [-1.25, 0.25]$, $q_k = [-0.75, 0.75]$, $q_l = [-0.9, 1.3]$ for the data at ambient pressure. The dispersionless nature of the triplet excitation in $\text{SrCu}_2(\text{BO}_3)_2$ renders a direct comparison between the mode positions in such two regions of Q a valid approach. The large integration ranges were required to improve the neutron counting statistics. The resulting spectra were fitted to Gaussian profiles with a sloping background and the fitted center positions yielded a shift of $\Delta E = -0.57(2)$ meV. Using the linear relation, $P = \frac{-\Delta E}{0.080(4)} \frac{\text{GPa}}{\text{meV}}$, between pressure and peak position given in Ref. 58 we obtain a pressure of $P = 0.7(1)$ GPa. At this pressure, the transition field to the 1/8 magnetization plateau is predicted to be 25 T [47, 48], which means that it is sufficiently suppressed to be probed at the HFM/EXED facility.

We now turn to finite magnetic fields where extensive diffraction data were collected at 20 T (34 h), 25 T (35 h) and 25.9 T (22 h). No magnetic-field-induced intensity was observed and we discuss the possible reasons for this further on. The inelastic signal at zero field and at 25.9 T is compared in Fig. 7(a)-(b). At zero field, the triplet excitation is located around 2.5 meV and it is almost dispersionless as expected. At 25.9 T, the triplet excitation is no longer observed and the spectrum is almost featureless. As a general

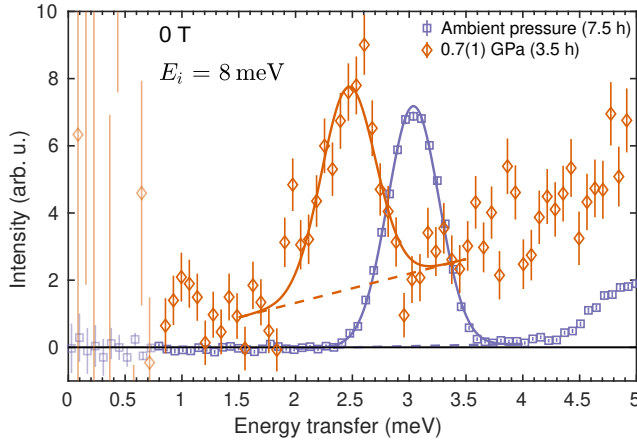


FIG. 6. Background-subtracted neutron intensity shown as a function of energy transfer at ambient and at finite pressure. At ambient pressure, the first triplet excitation is found around 3.0 meV and is shifted to lower energies upon applying pressure. The data are scaled such that the integrated intensities of the Gaussian fits (solid lines) are equal. The data points shown in lighter colors represent the limit of our resolution close to the elastic line. The ambient-pressure data are reproduced from Ref. 52.

observation in both cases, the neutron intensity is larger for larger $|\mathbf{Q}|$. Figure 7(c) shows the integrated neutron counts as a function of energy for the ranges $q_h = [-0.95, 0.55]$, $q_k = [-1.05, 0.45]$, $q_l = [-0.9, 1.3]$ for measurements with incoming energy $E_i = 8$ meV and $q_h = [-0.65, 0.35]$, $q_k = [-0.7, 0.3]$ and $q_l = [-0.65, 0.75]$ for measurements with incoming energy $E_i = 4$ meV. The scattering intensity at 25.9 T is smeared out, which results in a slightly higher overall count rate but with no clear features compared to the zero-field spectrum. The resolution is improved when collecting data using $E_i = 4$ meV, as shown in the inset of Fig. 7(c). Here, at zero field, the triplet mode is located at the edge of the accessible energy range and as a consequence its position is not well-determined. Nevertheless, it is clear that no new modes could be observed below the triplet at high fields.

We point out that the geometry of the HFM/EXED setup dictates that different values in E correspond to different values in q_l [52, 59]. This is not a problem in the particular case of $\text{SrCu}_2(\text{BO}_3)_2$ where the excitations are highly localized in all directions (and therefore show very little dispersion). In a system with more significant dispersion the approach of integrating over such a large volume of reciprocal space to improve the neutron statistics would be invalid.

We also note the spurious signal around 5.1 meV in Fig. 7(a)-(b). This signal does not come from the pressure cell, as it was also seen in the ambient-pressure experiment [52] but is most likely also not from the sample itself because the spurious position is independent of magnetic field and pressure. In the data measured with incoming energy $E_i = 4$ meV, a corresponding spurion appears around 2.1 meV. In the \mathbf{Q} -integrated data shown in Fig. 7(c), a Gaussian with a linear background was fitted to the zero-field data to describe the spurious signal and subsequently subtracted.

V. DISCUSSION

Our work underlines the challenge of performing neutron scattering experiments under the simultaneous application of several extreme conditions. We discuss below the performance of the bullet cell, interpret the results and suggest improvements for future designs. We point out that the discontinued operation of the BER-II research reactor at the HZB impeded thorough testing of the bullet cell using well-known samples as well as empty-cell measurements. This limited available beamtime meant that we aimed directly for doing a real experiment which in turn carries a higher risk due to more unknown variables. Nevertheless, we succeeded in measuring an inelastic neutron scattering signal under conditions of 25.9 T, 0.7(1) GPa and 200 mK.

Because of the stiffness of the $\text{SrCu}_2(\text{BO}_3)_2$ structure ($< 1\%$ reduction of lattice parameters in the (a, b) -plane at 5.5 GPa [60, 61] our pressure determination relies solely on the position of the triplet excitation of $\text{SrCu}_2(\text{BO}_3)_2$ in zero field together with its known evolution with pressure [58]. This is the main weakness of the setup and gives rise to a high uncertainty in the pressure determination. With the $1/8$ plateau extending for only a narrow field interval (around 1 T wide) at a given pressure [44, 47, 62], it is easy to overshoot or undershoot with the field. Below the $1/8$ plateau resides a spin-nematic phase [52], which is expected to be the ground state of the system at 25.9 T for pressures below 0.5 GPa [48]. The spectrum in the spin-nematic phase was previously characterized both experimentally and theoretically [52], and does not resemble the results in Figs. 7(b)-(c). On the other hand, if the pressure is higher than estimated, then at 25.9 T the system could already be on the next plateau where the magnetization is $2/15$ of the saturated moment. Future pressure cell designs for similar setups should include an independent pressure gauge such as Pb or NaCl for more accurate pressure determination and extensive offline testing should be undertaken using e.g. ruby fluorescence [63]. Other general improvements to consider for the bullet-cell design is strengthening the piston by using e.g. Zr-toughened alumina which also has high transparency to neutrons. Higher load-bearing capabilities may also be reached by adding a metallic binder around the cylinder of the piston. Finally, to address the issue of pressure loss upon cooling, incorporating a spring mechanism into the design could help maintain the force while cooling. This approach was successfully employed previously [64].

Whereas nuclear Bragg peaks from the sample were clearly visible, no magnetic-field-induced changes were observed in the neutron diffraction signal. This is expected in the spin-nematic phase at 20 T, where there is no long-range order. However, magnetic order is predicted at higher fields, i.e. both on the $1/8$ and $2/15$ plateaux [46] but we observed no magnetic Bragg peaks or diffuse magnetic intensity. There are a number of reasons for why such signal may not appear: (1) Truly two-dimensional order leads to rods of scattering. In the experiment, we bisect only a finite volume of the rods and do not capture the full scattering intensity. Consequently the magnetic signal could be too weak to be observed in this experiment. (2) We rely on model predictions for the choice of

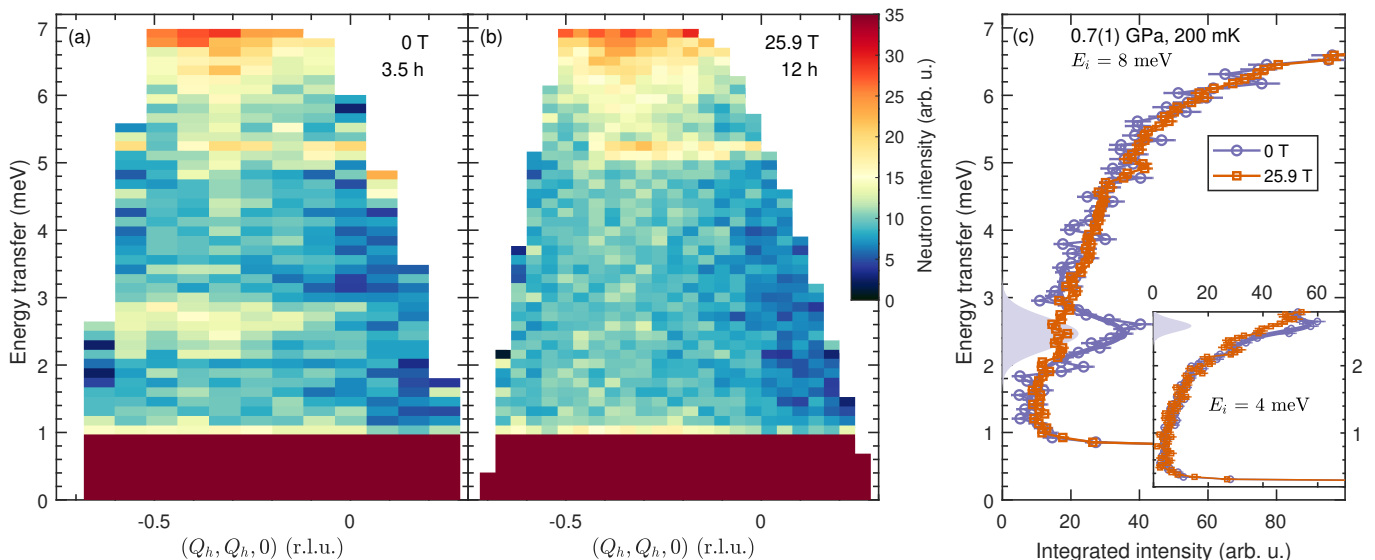


FIG. 7. **Inelastic neutron scattering spectra.** Neutron intensity at 0.7(1) GPa and 200 mK shown as a function of energy transfer and for $(q_h, q_h, 0)$ at (a) zero field and (b) 25.9 T measured with incoming energy $E_i = 8$ meV. The neutron intensity was integrated over ± 0.5 r.l.u. perpendicular to $(q_h, q_h, 0)$ and over the range $q_l = [-0.9, 1.3]$. (c) Neutron intensity integrated over the entire available volume of reciprocal space shown as a function of energy transfer for data collected with $E_i = 8$ meV for zero field (blue circles) and 25.9 T (red squares). The inset shows data with $E_i = 4$ meV. The triplet excitation is fitted to a Gaussian as described in the text and shown with blue shading.

Q range. If the model is wrong, we could simply be looking in the wrong part of reciprocal space. (3) The energy scale of the excitations on the plateau is likely lower compared to at zero field, which means that the temperature scale also decreases. Therefore, 200 mK might not be cold enough to enter the plateau.

In general, when magnetic fields stronger than around 16 T are required, the only option currently available for neutron scattering experiments is that of pulsed magnetic fields. With this method, field strengths up to 40 T may be reached [65–68], but only for a duration of a few milli seconds, which means a very short integrated measuring time. Consequently, this technique has to date only been suitable for diffraction studies where, as a rule, signals are orders of magnitudes stronger than inelastic signals. The pulsed-field path is therefore limited in applications and combinations with pressures and dilution temperatures have not been attempted. Conversely, the results presented here demonstrate the feasibility of pressure-cell engineering for horizontal magnets and may prove relevant for next-generation static magnets based on high- T_C superconducting ceramic materials and delivering beyond 16 T [69, 70]. Moreover, our experiment was carried out on a medium-flux reactor but the future European Spallation Source will provide orders of magnitude higher neutron flux which render neutron scattering experiments using a similar combination of extreme conditions for studying quantum magnetic systems promising. Until such time, the bullet-type pressure cells have potential for use with existing static horizontal-field magnets at various neutron facilities, in particular for combined pressure and field studies of spin textures with long periods such as skyrmions [71], vortex lattices [72] and spin spirals [73].

VI. CONCLUSIONS

We designed and constructed a pressure cell for neutron scattering experiments in combination with applied horizontal magnetic fields. Its bullet shape and optimized material choices enabled collection of inelastic neutron scattering and neutron diffraction data at 0.7(1) GPa, 25.9 T, and 200 mK. Under these conditions it was possible to investigate the $1/8$ magnetization plateau in the frustrated quantum magnet $\text{SrCu}_2(\text{BO}_3)_2$. Our work demonstrates the capabilities and future directions for combining the three extremes of high pressures, high magnetic fields and low temperatures for state-of-the-art neutron scattering experiments in the field of quantum magnetism.

ACKNOWLEDGMENTS

This work was funded by the European Research Council through the Synergy network HERO (Grant No. 810451) and by the Swiss National Science Foundation through Project Grant No. 188648. We would like to extend our gratitude to the team running the High Magnet Facility at the Helmholtz-Zentrum Berlin: many thanks to S. Gerischer, P. Heller, R. Wahle, S. Kempfer and P. Smeibidl for taking care of the dilution refrigerator and for making sure that the magnet was delivering its 25.9 T. E.F. is grateful to B. Normand for discussions and insight while shaping this work. K.K. would like to thank K. Kaneko (JAEA) for providing the information on sample environments at JRR-3.

DATA AVAILABILITY STATEMENT

Raw data were generated at the BER-II research reactor at the Helmholtz-Zentrum Berlin. Derived data supporting the findings of this study are available from the corresponding au-

thor upon reasonable request.

CONFLICT OF INTEREST STATEMENT

The authors have no conflicts to disclose.

-
- [1] S. Sachdev, "Quantum Criticality: Competing Ground States in Low Dimensions," *Science* **288**, 475–480 (2000).
- [2] A. Vasiliev, O. Volkova, E. Zvereva, and M. Markina, "Milestones of low-D quantum magnetism," *npj Quant. Mater.* **3**, 18 (2018).
- [3] A. T. Boothroyd, "Principles of Neutron Scattering from Condensed Matter," (2020).
- [4] C. Goodway and O. Kirichek, *Private communication*.
- [5] ISIS Neutron and Muon Source, "Sample environment page," (2022), access date: 2022-04-25.
- [6] Institute Laue-Langevin, "Sample environment page," (2022), access date: 2022-04-25.
- [7] R. Khasanov, R. Urquhart, M. Elender, and Konstantin Kamenev, "Three-wall piston-cylinder type pressure cell for muon-spinrotation/relaxation experiments," *High Press. Res.* **42**, 29–46 (2022).
- [8] Paul Scherrer Institute, "Sample environment page," (2022), access date: 2022-04-25.
- [9] N. Aso, T. Fujiwara, Y. Uwatoko, H. Miyano, and H. Yoshizawa, "Development of a hybrid CuBe/NiCrAl clamp-type high pressure cell for neutron diffraction," *J. Phys. Soc. Jpn.* **76**, 228–229 (2007).
- [10] K. Kaneko, C. Tabata, M. Hagihara, H. Yamauchi, Y. Oba, T. Kumada, M. Kubota, Y. Kojima, N. Nabatame, M. Sasaki, Y. Shimojo, K. Kodama, and T. Osakabe, "New Standard for Low Temperature Sample Environment at JAEA/JRR-3," *JPS Conf. Proc.* **41**, 011015 (2024).
- [11] T. Osakabe, K. Kuwahara, D. Kawana, K. Iwasa, D. Kikuchi, Y. Aoki, M. Kohgi, and H. Sato, "Pressure-Induced Antiferromagnetic Order in Filled Skutterudite $\text{PrFe}_4\text{P}_{12}$ Studied by Single-Crystal High-Pressure Neutron Diffraction," *J. Phys. Soc. Jpn.* **79**, 034711 (2010).
- [12] S. E. Dissanayake, M. Matsuda, K. Munakata, H. Kagi, J. Gouchi, and Y. Uwatoko, "Development of cubic anvil type high pressure apparatus for neutron diffraction," *J. Phys.: Condens. Matter* **31**, 384001 (2019).
- [13] K. Komatsu, K. Munakata, K. Matsubayashi, Y. Uwatoko, Y. Yokoyama, K. Sugiyama, and M. Matsuda, "Zr-based bulk metallic glass as a cylinder material for high pressure apparatuses," *High. Press. Res.* **35**, 54–262 (2015).
- [14] D. Kozlenko, S. Kichanov, E. Lukin, and B. Savenko, "The DN-6 Neutron Diffractometer for High-Pressure Research at Half a Megabar Scale," *Crystals* **8**, 331 (2018).
- [15] I. Mirebeau, I. N. Goncharenko, G. Dhalle, and A. Revcolevschi, "Pressure and Field Induced Magnetic Order in the Spin Liquid $\text{Tb}_2\text{Ti}_2\text{O}_7$ as Studied by Single Crystal Neutron Diffraction," *Phys. Rev. Lett.* **93**, 187204 (2004).
- [16] I. N. Goncharenko, "Neutron diffraction experiments in diamond and sapphire anvil cells," *High Press. Res.* **24**, 193–204 (2004).
- [17] O. Prokhnenko, W.-D. Stein, H.-J. Bleif, M. Fromme, M. Bartkowiak, and T. Wilpert, "Time-of-flight extreme environment diffractometer at the Helmholtz-Zentrum Berlin," *Rev. Sci. Instrum.* **86**, 033102 (2015).
- [18] P. Smeibidl, M. Bird, H. Ehmler, I. Dixon, J. Heinrich, M. Hoffmann, S. Kempfer, S. Bole, J. Toth, O. Prokhnenko, and B. Lake, "First hybrid magnet for neutron scattering at Helmholtz-Zentrum Berlin," *IEEE Trans. Appl. Supercond.* **26**, 4301606 (2016).
- [19] O. Prokhnenko, M. Bartkowiak, W.-D. Stein, N. Stuesser, H.-J. Bleif, M. Fromme, K. Prokes, P. Smeibidl, M. Bird, and B. Lake, "HFM-EXED - the high field facility for neutron scattering at HZB," *Proceedings of ICANS-XXI*, 278–285 (2016).
- [20] O. Prokhnenko, P. Smeibidl, W. D. Stein, M. Bartkowiak, and N. Stuesser, "HFM/EXED: The High Magnetic Field Facility for Neutron Scattering at BER II," *JLSRF* **3**, A115 (2017).
- [21] I. N. Goncharenko, I. Mirebeau, and A. Ochiai, "Magnetic neutron diffraction under pressures up to 43 GPa. Study of the EuX and GdX compounds," *Hyperfine Interact.* **128**, 225–244 (2001).
- [22] D. P. Kozlenko, I. Mirebeau, J.-G. Park, I. N. Goncharenko, S. Lee, J. Park, and B. N. Savenko, "High-pressure-induced spin-liquid phase of multiferroic YMnO_3 ," *Phys. Rev. B* **78**, 054401 (2008).
- [23] Ch. Rüegg, B. Normand, M. Matsumoto, A. Furrer, D. F. McMorro, K. W. Krämer, H.-U. Güdel, S. N. Gvasaliya, H. Mutka, and M. Boehm, "Quantum Magnets under Pressure: Controlling Elementary Excitations in TiCuCl_3 ," *Phys. Rev. Lett.* **100**, 205701 (2008).
- [24] N. Terada, C. V. Colin, N. Qureshi, T. C. Hansen, K. Matsubayashi, Y. Uwatoko, and A. A. Belik, "Pressure-induced incommensurate antiferromagnetic order in a ferromagnetic B-site ordered double-perovskite $\text{Lu}_2\text{NiMnO}_6$," *Phys. Rev. B* **102**, 094412 (2020).
- [25] E. Fogh, G. Giriat, M. E. Zayed, A. Piovano, M. Boehm, P. Steffens, I. Safiulina, U. B. Hansen, S. Klotz, J.-R. Soh, E. Pomjakushina, F. Mila, B. Normand, and H. M. Rønnow, "Spin waves and three-dimensionality in the high-pressure antiferromagnetic phase of $\text{SrCu}_2(\text{BO}_3)_2$," *Phys. Rev. Lett.* **133**, 246702 (2024).
- [26] S. Klotz, Th. Strässle, B. Lebert, M. d' Astuto, and Th. Hansen, "High pressure neutron diffraction to beyond 20 GPa and below 1.8 K using Paris-Edinburgh load frames," *High Press. Res.* **36**, 73–78 (2016).
- [27] V. F. Sears, "Neutron scattering lengths and cross sections," *Neutron News* **3**, 26–27 (1992).
- [28] S. Miyahara and K. Ueda, "Exact dimer ground state of the two-dimensional Heisenberg spin system $\text{SrCu}_2(\text{BO}_3)_2$," *Phys. Rev. Lett.* **82**, 3701 (1999).
- [29] B. S. Shastry and B. Sutherland, "Exact ground state of a quantum mechanical antiferromagnet," *Physica B+C* **108**, 1069 (1981).
- [30] H. Kageyama, K. Yoshimura, R. Stern, N. V. Mushnikov, K. Onizuka, M. Kato, K. Kosuge, C. P. Slichter, T. Goto, and Y. Ueda, "Exact dimer ground state and quantized magnetization plateaus in the two-dimensional spin system

- $\text{SrCu}_2(\text{BO}_3)_2$,” *Phys. Rev. Lett.* **82**, 3168 (1999).
- [31] H. Kageyama, M. Nishi, N. Aso, K. Onizuka, T. Yoshihama, K. Nukui, K. Kodama, K. Kakurai, and Y. Ueda, “Direct evidence for the localized single-triplet excitations and the dispersive multitriplet excitations in $\text{SrCu}_2(\text{BO}_3)_2$,” *Phys. Rev. Lett.* **84**, 5876 (2000).
- [32] H. Kageyama, K. Onizuka, Y. Ueda, M. Nohara, H. Suzuki, and H. Takagi, “Low-temperature specific heat study of $\text{SrCu}_2(\text{BO}_3)_2$ with an exactly solvable ground state,” *J. Exp. Theor. Phys.* **90**, 129 (2000).
- [33] B. D. Gaulin, S. H. Lee, S. Haravifard, J. P. Castellan, A. J. Berlinsky, H. A. Dabkowska, Y. Qiu, and J. R. D. Copley, “High-resolution study of spin excitations in the singlet ground state of $\text{SrCu}_2(\text{BO}_3)_2$,” *Phys. Rev. Lett.* **93**, 267202 (2004).
- [34] K. Kakurai, K. Nukui, N. Aso, M. Nishi, H. Kadowaki, H. Kageyama, Y. Ueda, L.-P. Regnault, and O. Cépas, “Neutron Scattering Investigation on Quantum Spin System $\text{SrCu}_2(\text{BO}_3)_2$,” *Progress of Theoretical Physics Supplement* **159**, 22 (2005).
- [35] A. Koga and N. Kawakami, “Quantum Phase Transitions in the Shastry-Sutherland Model for $\text{SrCu}_2(\text{BO}_3)_2$,” *Phys. Rev. Lett.* **84**, 4461–4464 (2000).
- [36] C. H. Chung, J. B. Marston, and S. Sachdev, “Quantum phases of the Shastry-Sutherland antiferromagnet: Application to $\text{SrCu}_2(\text{BO}_3)_2$,” *Phys. Rev. B* **64**, 134407 (2001).
- [37] A. Läuchli, S. Wessel, and M. Sigrist, “Phase diagram of the quadrumerized Shastry-Sutherland model,” *Phys. Rev. B* **66**, 014401 (2002).
- [38] P. Corboz and F. Mila, “Tensor network study of the Shastry-Sutherland model in zero magnetic field,” *Phys. Rev. B* **87**, 115144 (2013).
- [39] H. Nakano and T. Sakai, “Third Boundary of the Shastry-Sutherland Model by Numerical Diagonalization,” *J. Phys. Soc. Jpn.* **87**, 123702 (2018).
- [40] N. Xi, H. Chen, Z. Y. Xie, and R. Yu, “Plaquette valence bond solid to antiferromagnet transition and deconfined quantum critical point of the Shastry-Sutherland model,” *Phys. Rev. B* **107**, L220408 (2023).
- [41] K. Onizuka, H. Kageyama, Y. Narumi, K. Kindo, Y. Ueda, and T. Goto, “1/3 magnetization plateau in $\text{SrCu}_2(\text{BO}_3)_2$ - stripe order of excited triplets -,” *J. Phys. Soc. Jpn.* **69**, 1016 (2000).
- [42] M. Takigawa, M. Horvatić, T. Waki, S. Krämer, C. Berthier, F. Lévy-Bertrand, I. Sheikin, H. Kageyama, Y. Ueda, and F. Mila, “Incomplete Devil’s Staircase in the Magnetization Curve of $\text{SrCu}_2(\text{BO}_3)_2$,” *Phys. Rev. Lett.* **110**, 067210 (2013).
- [43] Y. H. Matsuda, N. Abe, S. Takeyama, H. Kageyama, P. Corboz, A. Honecker, S. R. Manmana, G. R. Foltin, K. P. Schmidt, and F. Mila, “Magnetization of $\text{SrCu}_2(\text{BO}_3)_2$ in Ultrahigh Magnetic Fields up to 118 T,” *Phys. Rev. Lett.* **111**, 137204 (2013).
- [44] Z. Shi, S. Dissanayake, P. Corboz, W. Steinhardt, D. Graf, D. M. Silevitch, H. A. Dabkowska, T. F. Rosenbaum, F. Mila, and S. Haravifard, “Discovery of quantum phases in the Shastry-Sutherland compound $\text{SrCu}_2(\text{BO}_3)_2$ under extreme conditions of field and pressure,” *Nat. Commun.* **13**, 2301 (2022).
- [45] T. Nomura, P. Corboz, A. Miyata, S. Zherlitsyn, Y. Ishii, Y. Kohama, Y. H. Matsuda, A. Ikeda, C. Zhong, H. Kageyama, and F. Mila, “Unveiling new quantum phases in the Shastry-Sutherland compound $\text{SrCu}_2(\text{BO}_3)_2$ up to the saturation magnetic field,” *Nat. Commun.* **14**, 3769 (2023).
- [46] P. Corboz and F. Mila, “Crystals of bound states in the magnetization plateaus of the Shastry-Sutherland model,” *Phys. Rev. Lett.* **112**, 147203 (2014).
- [47] S. Haravifard, D. Graf, A. E. Feiguin, C. D. Batista, J. C. Lang, D. M. Silevitch, G. Srajer, B. D. Gaulin, H. A. Dabkowska, and T. F. Rosenbaum, “Crystallization of spin superlattices with pressure and field in the layered magnet $\text{SrCu}_2(\text{BO}_3)_2$,” *Nat. Commun.* **7**, 11956 (2016).
- [48] D. A. Schneider K. Coester F. Mila and K. P. Schmidt, “Pressure dependence of the magnetization plateaus of $\text{SrCu}_2(\text{BO}_3)_2$,” *Phys. Rev. B* **93**, 241107(R) (2016).
- [49] H. Kageyama, K. Onizuka, T. Yamauchi, and Y. Ueda, “Crystal growth of the two-dimensional spin gap system $\text{SrCu}_2(\text{BO}_3)_2$,” *J. Cryst. Growth* **206**, 65–67 (1999).
- [50] G. Jorge, M. Jaime, N. Harrison, R. Stern, H. Dabkowska, and B. D. Gaulin, “High magnetic field magnetization and specific heat of the 2D spin-dimer system $\text{SrCu}_2(\text{BO}_3)_2$,” *J. Alloys Compd.* **369**, 90–92 (2004).
- [51] M. Bartkowiak, K. Prokeš, M. Fromme, A. Budack, J. Dirlick, and O. Prokhnenko, “Exeq and ineq: software tools for experiment planning at the extreme environment diffractometer,” *J. Appl. Cryst.* **53**, 1613–1619 (2020).
- [52] E. Fogh, M. Nayak, O. Prokhnenko, M. Bartkowiak, K. Munakata, J.-R. Soh, A. A. Turrini, M. E. Zayed, E. Pomjakushina, H. Kageyama, H. Nojiri, K. Kakurai, B. Normand, F. Mila, and H. M. Rønnow, “Field-induced bound-state condensation and spin-nematic phase in $\text{SrCu}_2(\text{BO}_3)_2$ revealed by neutron scattering up to 25.9 T,” *Nat. Commun.* **15**, 442 (2024).
- [53] S. Klotz, *Techniques in High Pressure Neutron Scattering* (Taylor & Francis / CRC Press, Boca Raton, 2013).
- [54] Z. Ma, J. Lass, D. G. Mazzone, G. Simutis, S. Thürsam, T. Fennell, E. Pomjakushina, M. Bartkowiak, S. Nikitin, M. Bertelsen, P. Willendrup, U. Filges, and C. Klauser, “Sourcing and reducing sample environment background in low-temperature high-pressure neutron scattering experiments,” *Nucl. Instrum. Methods Phys. Res. A* **1066**, 169634 (2024).
- [55] M. Bertelsen, *Software for simulation and design of neutron scattering instrumentation*, Ph.D. thesis, University of Copenhagen (2017).
- [56] P. Willendrup and K. Lefmann, “McStas (i): Introduction, use, and basic principles for ray-tracing simulations,” *J. Neutron Res.* **22**, 1–16 (2020).
- [57] P. Willendrup and K. Lefmann, “McStas (ii): An overview of components, their use, and advice for user contributions,” *J. Neutron Res.* **23**, 7–27 (2021).
- [58] M. E. Zayed, Ch. Rüegg, Th. Strässle, U. Stühr, B. Roessli, M. Ay, J. Mesot, P. Link, E. Pomjakushina, M. Stingaciu, K. Conder, and H. M. Rønnow, “Correlated decay of triplet excitations in the Shastry-Sutherland compound $\text{SrCu}_2(\text{BO}_3)_2$,” *Phys. Rev. Lett.* **113**, 067201 (2014).
- [59] S. Allenspach, A. Madsen, A. Biffin, M. Bartkowiak, O. Prokhnenko, A. Gazizulina, X. Liu, R. Wahle, S. Gerischer, S. Kempfer, P. Heller, P. Smeibidl, A. Mira, N. Laflorencie, F. Mila, B. Normand, and Ch. Rüegg, “Investigating field-induced magnetic order in Han purple by neutron scattering up to 25.9 T,” *Phys. Rev. B* **106**, 104418 (2022).
- [60] I. Loa, F.X. Zhang, K. Syassen, P. Lemmens, W. Crichton, H. Kageyama, and Y. Ueda, “Crystal structure and lattice dynamics of $\text{SrCu}_2(\text{BO}_3)_2$ at high pressures,” *Physica B* **359-361**, 980–982 (2005).
- [61] S. Haravifard, A. Banerjee, J. van Wezel, D. M. Silevitch, A. M. dos Santos, J. C. Lang, E. Kermarrec, G. Srajer, B. D. Gaulin, J. J. Molaison, H. A. Dabkowska, and T. F. Rosenbaum, “Emergence of long-range order in sheets of magnetic dimers,” *Proc. Natl. Acad. Sci.* **111**, 14372–14377 (2014).
- [62] F. Levy, I. Sheikin, C. Berthier, M. Horvatić, M. Takigawa, H. Kageyama, T. Waki, and Y. Ueda, *EPL* **81**, 67004 (2008).
- [63] H. K. Mao, J. Xu, and P. M. Bell, “Calibration of the Ruby PressureGauge to 800 kbar Under Quasi-

- Hydrostatic Conditions,” *J. Geophys. Res.* **91**, 673–4676 (1986).
- [64] B. Haberl, S. Dissanayake, Y. Wu, D. A. A. Myles, A. M. dos Santos, M. Loguillo, G. M. Rucker, D. P. Armitage, M. Cochran, K. M. Andrews, C. Hoffmann, H. Cao, M. Matsuda, F. Meilleur, F. Ye, J. J. Molaison, and R. Boehler, “Next-generation diamond cell and applications to single-crystal neutron diffraction,” *Rev. Sci. Instrum.* **89**, 092902 (2018).
- [65] F. Duc, X. Tonon, J. Billette, B. Rollet, W. Knafo, F. Bourdarot, J. Béard, F. Mantegazza, B. Longuet, J. E. Lorenzo, E. Lelièvre-Berna, P. Frings, and L.-P. Regnault, “40-Tesla pulsed-field cryomagnet for single crystal neutron diffraction,” *Rev. Sci. Instrum.* **89**, 053905 (2018).
- [66] E. Fogh, T. Kihara, R. Toft-Petersen, M. Bartkowiak, Y. Narumi, O. Prokhnenko, A. Miyake, M. Tokunaga, K. Oikawa, M. K. Sørensen, J. C. Dyrnum, H. Grimmer, H. Nojiri, and N. B. Christensen, “Magnetic structures and quadratic magnetoelectric effect in LiNiPO_4 beyond 30 T,” *Phys. Rev. B* **101**, 024403 (2020).
- [67] A. Gazizulina, D. L. Quintero-Castro, Z. Wang, F. Duc, F. Bourdarot, K. Prokes, W. Schmidt, R. Daou, S. Zherlitsyn, N. Islam, N. H. Kolnes, A. B. Kademane, A. Schilling, and B. Lake, “Neutron diffraction of field-induced magnon condensation in the spin-dimerized antiferromagnet $\text{Sr}_3\text{Cr}_2\text{O}_8$,” *Phys. Rev. B* **104**, 064430 (2021).
- [68] S. Holm-Janass, M. Akaki, E. Fogh, T. Kihara, M. D. Le, P. C. Forino, S. E. Nikitin, T. Fennell, A. Painganoor, D. Vaknin, M. Watanabe, N. B. Christensen, H. Nojiri, and R. Toft-Petersen, “Magnetic structure and magnetoelectric properties of the spin-flop phase in LiFePO_4 ,” *Phys. Rev. B* **109**, 174413 (2024).
- [69] W. D. Markiewicz, D. C. Larbalestier, H. W. Weijers, A. J. Vorum, K. W. Pickard, W. R. Sheppard, J. Jaroszynski, A. Xu, R. P. Walsh, J. Lu, A. V. Gavrilin, and P. D. Noyes, “Design of a Superconducting 32 T Magnet With REBCO High Field Coils,” *IEEE Trans. Appl. Supercond.* **22**, 4300704 (2012).
- [70] H. Bai, M. D. Bird, L. D. Cooley, I. R. Dixon, K. L. Kim, D. C. Larbalestier, W. S. Marshall, U. P. Trociewitz, H. W. Weijers, D. V. Abaimov, and G. S. Boebinger, “The 40 T Superconducting Magnet Project at the National High Magnetic Field Laboratory,” *IEEE Trans. Appl. Supercond.* **30**, 4300405 (2020).
- [71] S. Mühlbauer, B. Binz, F. Jonietz, C. Pfleiderer, A. Rosch, A. Neubauer, R. Georgii, and P. Böni, “Skyrmion Lattice in a Chiral Magnet,” *Science* **323**, 915–919 (2009).
- [72] Y. Xie, N. Chalus, Z. Wang, W. Yao, J. Liu, Y. Yao, J. S. White, L. M. DeBeer-Schmitt, J.-X. Yin, P. Dai, and M. R. Eskildsen, “Conventional superconductivity in the doped kagome superconductor $\text{Cs}(\text{V}_{0.86}\text{Ta}_{0.14})_3\text{Sb}_5$ from vortex lattice studies,” *Nat. Commun.* **15**, 6467 (2024).
- [73] A. Romaguera and M. Medarde, “Room temperature magnetoelectric magnetic spirals by design,” *Front. Mater.* **11**, 144876 (2024).